



Research Article

Enhanced helium ion irradiation tolerance in a Fe-Co-Ni-Cr-Al-Ti high-entropy alloy with L1₂ nanoparticlesY.L. Zhao^{a,*}, F.L. Meng^b, T. Yang^c, J.H. Luan^c, S.F. Liu^d, G.M. Yeli^e, W.T. Lin^d, W.H. Liu^a, X.J. Liu^a, C.T. Liu^c, J.J. Kai^d^a School of Materials Science and Engineering, Harbin Institute of Technology (Shenzhen), Shenzhen 518055, China^b School of Materials Science and Engineering, Southern University of Science and Technology, Shenzhen 518055, China^c Department of Materials Science and Engineering, Mechanical Behavior Division of Shenyang National Laboratory for Materials Science, City University of Hong Kong, Hong Kong, China^d Department of Mechanical Engineering, City University of Hong Kong, Hong Kong, China^e Institute of Nuclear & New Energy Technology, Tsinghua University, Beijing 100084, China

ARTICLE INFO

Article history:

Received 15 June 2022

Revised 9 August 2022

Accepted 19 September 2022

Available online 19 November 2022

Keywords:

L1₂ nanoparticles

High-entropy alloy

Helium bubble

Phase stability

Radiation-induced segregation

ABSTRACT

L1₂-strengthened high entropy alloys (HEAs) with excellent room and high-temperature mechanical properties have been proposed as promising candidates as structural materials for advanced nuclear systems. However, knowledge about their radiation response is fairly limited. In the present work, a novel HEA with a high density of L1₂ nanoparticles was irradiated with He ion at 500 °C. Transmission electron microscope (TEM) and atom probe tomography (APT) were employed to study the evolution of microstructural stability and radiation-induced segregation. Similar to the single-phase FeCoNiCr HEA, the main microstructural features were numerous large faulted dislocation loops and helium bubbles. While the irradiation resistance of the present L1₂-strengthened HEA is much improved in terms of reduced bubble size, which could be attributed to the considerable He trapping efficiency of the coherent precipitate/matrix interface and the enhanced capability of the interface for damage elimination when the matrix channel width is narrow. APT analysis revealed that an inverse-Kirkendall-mechanism-dominated radiation-induced segregation (RIS) occurs around bubbles, where a significant Co enrichment and Ni depletion can be clearly observed. In addition, the competing dynamics of ballistic mixing and elemental clustering that raised from the irradiation-enhanced diffusion in a highly supersaturated matrix, along with the low precipitation nucleation barrier due to the small lattice misfit, lead to a dynamical precipitation dissolution and re-precipitation appears under irradiation. Such a promising phenomenon is expected to promote a potential self-healing effect and could in turn provide a sustainable irradiation tolerance over the operational lifetime of a reactor.

© 2023 Published by Elsevier Ltd on behalf of The editorial office of Journal of Materials Science & Technology.

1. Introduction

The increasing demand for clean energy requires the accelerated development of new materials for advanced Gen-IV nuclear reactors, in which materials are designed to face harsher environments with increased temperatures, more intense radiation flux, and corrosive coolants [1,2]. High-entropy alloys (HEAs) composed of multiple principal elements have recently garnered extensive interest due to their numerous superior properties in comparison to conventional alloys, such as excellent mechanical properties [3–6], corrosion resistance [7,8], and encouraging irradiation tolerance

[9–11], which shows a great potential to serve as promising structural materials for advanced nuclear energy systems.

It is well-established that materials subjected to irradiation undergo serious structural damage that can result in severe performance degradation. In general, introducing a high density of defect sinks can effectively alleviate damage accumulation and enhance the irradiation tolerance of the materials [12–15]. This has been widely used in many traditional materials, such as nano-grained and multi-nanolayer materials [12], nanoporous materials [13], and oxide-dispersion-strengthened steels [14,15]. In contrast, single-phase HEAs present a novel approach to reducing defect damage due to their unique defect evolution that arises from chemical complexity as well as the local lattice distortion [9,16–18]. Specifically, early experimental and simulation studies demonstrated that

* Corresponding author.

E-mail address: zhaoyilu@hit.edu.cn (Y.L. Zhao).

the increased compositional complexity of HEAs can effectively reduce interstitial mobility and enhance vacancy-interstitial recombination, leading to improved swelling resistance and delayed dislocation loop growth [19]. Similar results were also observed in a series of multicomponent alloys under Ni^{2+} -irradiation at 500 °C [20]. The results showed that the transition of faulted dislocation loops to full dislocation loops could be suppressed as the compositional complexity increase from NiFe, NiCoFe, NiCoFeCr to NiCoFeCrMn [20]. Additionally, He et al. [21] studied the defect structure of FeCoCrNi HEA irradiated with high energy electrons at 400 °C and found that the growth of dislocation loops in the FeCoCrNi HEA was 40 times slower than that in pure Ni.

Although favorable irradiation tolerance has been demonstrated on several single-phase HEAs, especially the Ni-concentrated HEAs, most of their strengths are unsatisfactory at elevated temperatures that could encounter in advanced nuclear reactors [22]. More recently, HEAs strengthened by L_{12} nanoparticles have attracted increasing attention for their superior room and high-temperature mechanical properties [23–25]. Yang et al. [23] designed novel HEAs with high-density nanosized L_{12} particles through delicately compositional and microstructural tuning. The resulting HEAs show a superior combination of mechanical properties, i.e., strengthening to GPa strength with even improved ductility as compared to their single-phase counterparts. We recently demonstrated that Nb-bearing L_{12} -strengthened HEAs can maintain high strengths at temperatures up to 870 °C, which outperforms most of the HEAs and many commercial superalloys [26]. More importantly, Du et al. [27] showcased a reversible-and-rapid local disordering-ordering transition of the high-density superlattice nanoprecipitates in metallic materials (e.g., B2 nanoparticles in the $\text{Fe}_{75}\text{Ni}_{18}\text{Al}_3\text{Mo}_4$ martensitic steel) under heavy ion irradiation at elevated temperatures. Such a dynamic process can effectively eliminate the radiation-involved damage, leading to an extraordinarily high irradiation tolerance. Nevertheless, studies on the irradiation response of those HEAs with attractive mechanical properties are still fairly limited.

In addition to the excellent mechanical properties, L_{12} -strengthened HEAs exhibit encouraging indications for improving irradiation resistance. On one hand, the face-centered-cubic (FCC) matrix can, to some extent, maintain the advantage of chemical complexity (solid-solution phase) for irradiation improvement [28,29]. On the other hand, the L_{12} nanoparticles may further serve as potential defect sinks to reduce structural damage, resulting in an enhanced irradiation tolerance [30]. In particular, those particles may potentially provide He trapping and bubble nucleation sites, which mitigate helium accumulation and the associated detrimental effect on the mechanical properties in terms of swelling, hardening, and embrittlement [31]. Helium-induced degradation of mechanical properties is one of the most daunting and important challenges for advanced fission and proposed fusion energy systems. Therefore, knowledge about the irradiation performance of the He-irradiated L_{12} -strengthened HEAs at elevated temperatures is of great interest and technological importance, which is far from being exploited.

In the present study, an L_{12} -strengthened HEA with a nominal composition of $\text{Ni}_{30}\text{Co}_{30}\text{Fe}_{13}\text{Cr}_{15}\text{Al}_6\text{Ti}_6$ (at.%, denoted as Al6Ti6 hereafter) was helium-irradiated at 500 °C. The initial structure and the detailed thermomechanical process of the material are described in Ref. [32]. The volume fraction of the L_{12} phase was determined to be about 37.3% with an average particle size of 29 ± 5 nm. The irradiation responses including the bubble formation, the structural damage, the radiation-induced segregation (RIS), and the phase stability were systemically evaluated. The effect of the L_{12} -nanoparticles on the He entrapment was further carefully discussed.

2. Experimental

Prior to irradiation, all the samples were mechanically and chemically polished to achieve a mirror-like finish surface. Irradiation was carried out at the Accelerator Laboratory of the National Tsing Hua University. The well-polished specimens were irradiated by 275 keV He ions under a vacuum of 5×10^{-5} Pa to a total fluence of 6.4×10^{20} ions/ m^2 at 500 °C. The corresponding irradiation-induced damage profile with the variation of implanted depth was calculated using the Stopping and Range of Ions in Matter (SRIM-2013) [33] with the Quick Kinchin-Pease Mode and the displacement threshold energy was set to 40 eV for all elements [34].

Cross-sectional specimens for transmission electron microscope (TEM, JEOL JEM-2100F) and atom probe specimens were fabricated using a dual-beam scanning electronic microscope (SEM)/focused-ion-beam (FIB) instrument. The elemental mapping was carried out using an FEI Talos F200X S/TEM equipped with Super-X energy-dispersive X-ray spectroscopy (EDS). The APT analysis was conducted using the CAMECA LEAP 5000 XR system with a detection rate of 0.002 atoms per pulse. The specimen was conducted in the voltage mode at 65 K with a pulse repetition rate of 200 kHz. The APT data were reconstructed and analyzed using the CAMECA Integrated Visualization and Analysis Software (IVAS) 3.8.2.

3. Results and discussion

3.1. Structural damage

Fig. 1(a) presents the depth-dependent profile of He concentration and irradiation dose (in the unit of displacements per atom, dpa) predicted by the SRIM software. The damage dose approaches a maximum of ~ 1.6 dpa at ~ 600 nm and the peak He concentration reaches ~ 3.5 at.% at depth of ~ 650 nm. The corresponding panoramic view of the cross-sectional TEM sample for the irradiated HEA is shown in Fig. 1(b). A significant variation in the bubble density with the distance from the implantation surface was observed. A further close-up of a typical damage region (Fig. 1(c)) was acquired by the Fresnel-contrast analysis in an under-focus TEM image [35], showing numerous helium nanobubbles and faulted dislocation loops (faint fringe contrast) distributed as the dominated structural damage. The bubble size distribution was statistically analyzed from at least three different regions at the same depth, as can be seen in Fig. 1(d). The averaged bubble size (in diameters) in the He peak region is 3.0 ± 0.62 nm, which is $\sim 17\%$ smaller than that of the single-FCC FeCoNiCr HEA without nanoparticles under the same irradiation condition (275 keV He^+ ions with a fluence of $6.4 \times 10^{20} \text{ m}^{-2}$ at 773 K) [36], demonstrating an improved damage resistance of the present precipitation-strengthened HEA.

Irradiation-induced dislocation loops are prevalent in metallic alloys, which often bring about an irradiation hardening effect and seriously embrittle material [31]. Similar to the previous results where faulted loops rather than full dislocations loops prevail in the concentrated HEA [20], large edge-on faulted dislocation loops with a maximum size of ~ 300 nm can be evidently imaged in bright-field (BF) TEM image, as marked by yellow arrows in Fig. 2(a). The rel-rods dark-field (DF) TEM image [37] was further applied to characterize the distribution of the faulted loops, where strongly depth-dependent distribution of the faulted dislocation loops can be clearly observed, i.e., the number density of the faulted dislocation loops increases from the sample surface to the irradiation affected region. Interestingly, there is a strong strain field characterized by the dark-ring contrast surrounding the nanobubbles (highlighted by red arrows). Such a dark-ring contrast varies with tilting conditions and is independent of the fo-

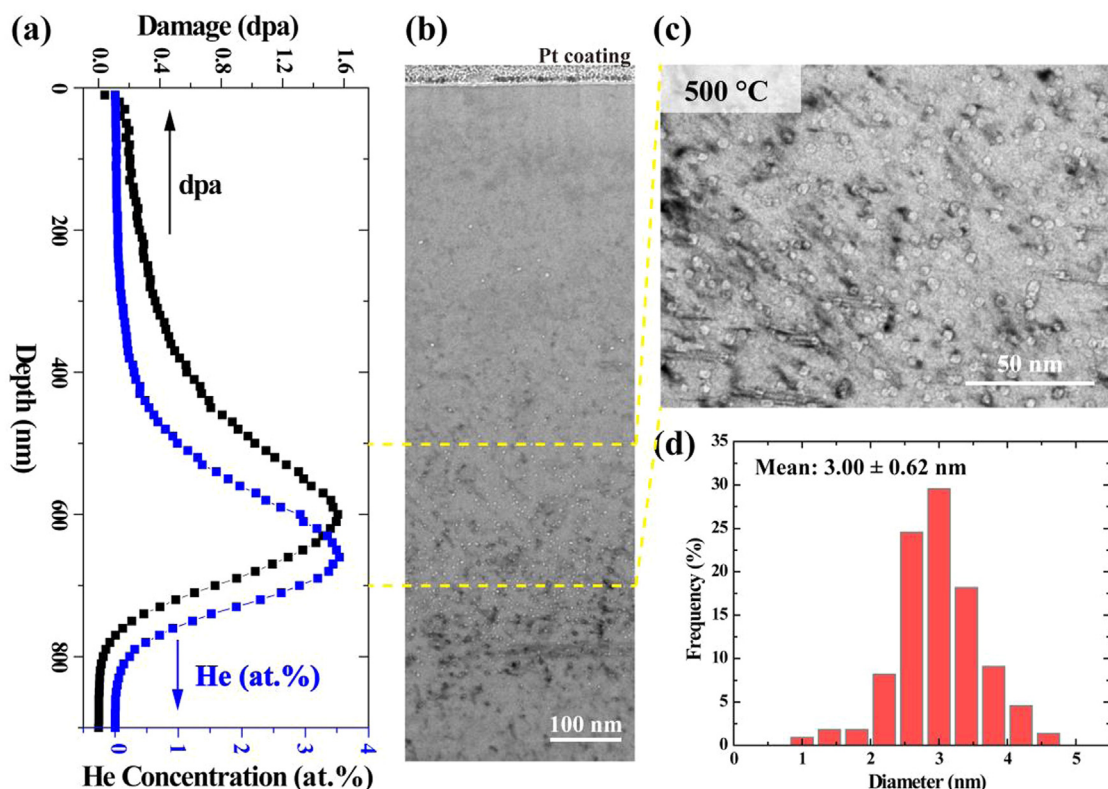


Fig. 1. (a) Predicted depth-dependent profile of He concentration and irradiation dose. (b) Corresponding bright-field TEM image of the cross-sectional TEM sample for the Al6Ti6 HEA irradiated at 500 °C. (c) A representative enlarged view required in an under-focused condition showing the distribution of He bubbles at the irradiation depth of 500–700 nm. (d) Size distribution of the bubbles at peak He concentration region.

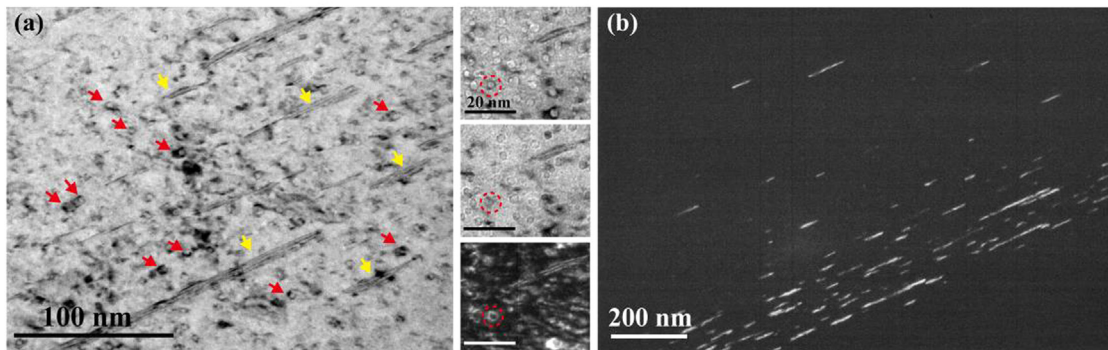


Fig. 2. Representative (a) BF-TEM image showing numerous faulted dislocation loops in the He ion irradiated Al6Ti6 HEA. Enlarged views with under-focus, over-focus, and the corresponding weak-beam dark-field images on the right column demonstrating the strain field around the nanobubbles. (b) Relrod DF-TEM image showing the faulted loops.

cus condition. A typical example is shown in the right column in Fig. 2(a). The upper two TEM images with Fresnel contrast (under-focus and over-focus) demonstrate the location of the nanobubble. Clearly, the surrounding region of the nanobubble is enlightened in the corresponding weak-beam dark-field image as the strain field causes the region at the Bragg condition. This could be attributed to the high pressure inside the bubbles [38] or the segregation-induced lattice mismatch between the matrix and the segregation regions. Such over-pressurized bubbles could result in a bias for vacancies capture [39] of the bubbles and thus influence the RIS behaviors [38].

3.2. Phase stability of the L_{12} precipitates

To reveal the phase stability of the present Al6Ti6 HEA under He ion irradiation at 500 °C, the distributions of ordered L_{12}

nanoparticles after irradiation were evaluated through the combined TEM and APT analyses [40]. Fig. 3 shows the representative DF-TEM images of the L_{12} nanoparticles acquired from regions subjected to different irradiation doses, with the corresponding selected area diffraction patterns (SADPs) along the $\langle 112 \rangle$ zone axis shown in the bottom column. The denoted dose values were derived from the SRIM calculation, i.e., ~ 0.2 dpa represents the region near the surface and ~ 1.6 dpa corresponds to the peak damage region at the depth between 500 and 700 nm. The characterizations of the 0 dpa region, both the DF-TEM image and the SADP, were taken from the depth region beyond 1.5 μm , where thermal rather than irradiation effect on the microstructures involved. The results clearly show that the gradual shrinkage of the ordered L_{12} nanoparticles as the dose level increases, which together with the gradually faded superlattice diffraction spots (indicated as yellow dashed circles) in the SADPs demonstrate that

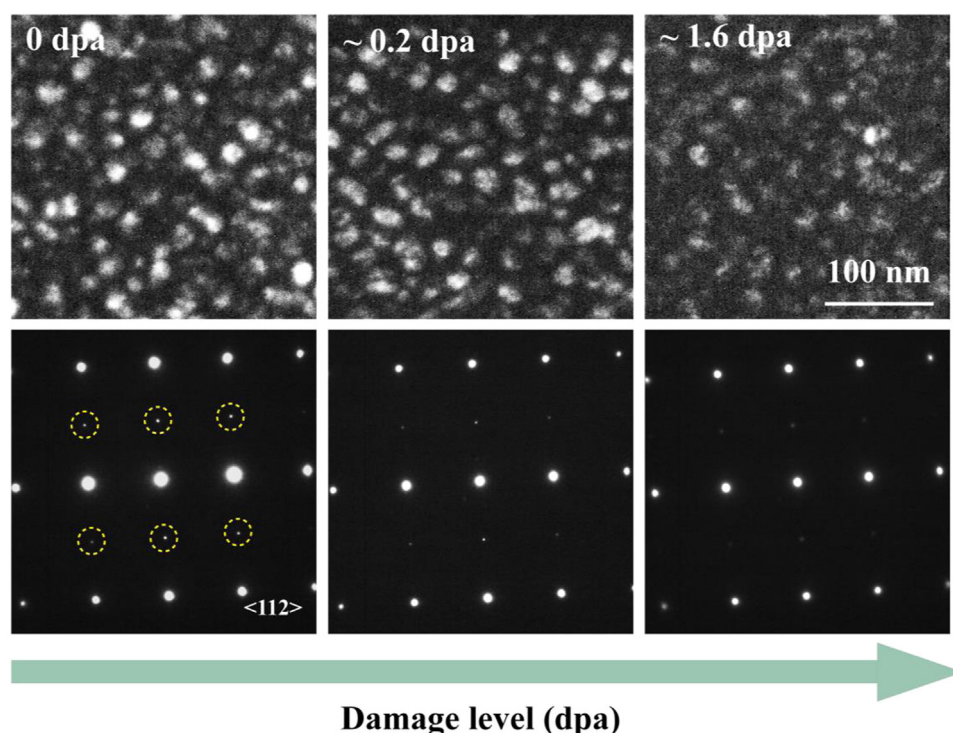


Fig. 3. DF-TEM images exhibiting the evolution of the L_{12} precipitation with the variation of damage levels. The corresponding SADPs along the $\langle 112 \rangle$ zone axis are shown in the bottom column.

the ordered nanoparticle tend to be dissolved under irradiation. Also, it is well documented that the relative ratio of superlattice to fundamental reflection intensity, e.g., I_{110}/I_{220} , has an approximation relationship with the ordering parameter (S) of an L_{12} ordered crystal, i.e., $S^2 \propto I_{110}/I_{220}$ [41]. For further verification, the intensity ratios of $R(I_{110}/I_{220})$ were measured from the intensity profiles via Gatan DigitalMicrograph software. The results show that $R_0 > R_{0.2} > R_{1.6}$, where the subscripts represent the dose level. The gradually diminished intensity ratio again could be indicative of the decreased ordering degree due to the dissolution of ordered nanoparticles. In other words, the irradiation-induced disordering of the ordered nanoparticles occurs in the present HEA.

Fig. 4(a) reconstructs a typical APT needle taken from the peak damage region. An isosurface of 40 at.% Ti+Ni (in green) was used to delineate the ordered nanoparticles. Interestingly, despite slightly distorted nanoparticles, numerous fine clusters enriched with Al and Ni (~ 1 nm in radius) were evidently observed inside the FCC matrix, highlighted by an isosurface of 28 at.% Al+Ni (in blue). For comparison, the underneath unirradiated region (0 dpa, far away from the irradiated surface) was also characterized by APT to clarify the equivalent effect of thermal annealing at 500 °C (Fig. 5). The resulting chemical constitutions of both L_{12} nanoparticles and FCC matrix are identical to the pristine sample reported by Yang et al. [32]. No clusters can be found in the unirradiated region, demonstrating the high thermal stability of the present alloy.

Furthermore, the compositional proxigrams of the nanoparticles and the clusters in the peak damaged region are shown in Fig. 4(b, c), respectively. Noting that the (Ni+Co) concentration in the cluster core is about triple that of the (Al+Ti) concentration. Such chemical constitutions of the clusters are quite close to the equilibrium A_3B -type L_{12} nanoparticles, implying a high ordering propensity of those clusters. That is to say, re-precipitation of the L_{12} nanoparticles could occur during the irradiation process. Similar results have also been observed in previous studies when L_{12} -strengthened HEA was irradiated using 6.4 MeV Fe^{3+} [42]. For the

pre-existing nanoparticles, the compositional proxigram shows an evident elemental re-distribution (Fig. 4(c)). In general, it seems that FCC-forming elements like Co, Fe, and Cr elements strongly segregate to the phase boundary while the L_{12} -forming element Ni largely runs away from the phase boundary. Whereas Al and Ti are slightly depleted in the interphase region. Further quantitative analysis revealed that the L_{12} nanoparticles after irradiation consist of 55.1 at.% Ni, 16.7 at.% Co, 13.5 at.% Ti, 10.7% Al, 2.1 at.% Fe, and 1.9 at.% Cr. In contrast, the nanoparticles in the unirradiated region (0 dpa) consist of less Ni (50.1 at.%), more Co (20.0 at.%), slightly more Fe (3.3 at.%) and Cr (2.5 at.%), and close Ti (13.6 at.%) and Al (10.5 at.%) concentration (see Fig. 5). The results are suggested that He ion irradiation is likely to eventually drain Co, Fe, and Cr elements out of the L_{12} particles. This is distinguished from the heavy-ion-irradiation scenario where the element mixture is significant due to ballistic mixing, and more matrix elements (Fe, Cr, and Co elements) tend to diffuse into the particles [42]. Consequently, a blurry interface between particles and the matrix would be observed [42].

3.3. Bubble entrapment and radiation-induced segregations

This variation appears to be due to the He-induced heterogeneity of defect dynamics [38,43], which is correlated to the bubble distribution and the associated RIS effect. Scanning transmission electron microscopy (STEM) analysis coupled with EDS maps (Fig. 6) of the individual elements provides insight into the local RIS effects at the bubbles. A strong RIS of Co at the bubbles can be clearly observed, highlighted by the red/blue dashed circles in both the BF-STEM image and the elemental map of Co (Fig. 6). More importantly, despite a few bubbles in the precipitates (blue dashed circle), most of the bubbles appear to be entrapped at the phase boundary of the L_{12} precipitates, suggesting that the precipitates/matrix interface can act as effective trapping sites for He atoms and bubble nucleation.

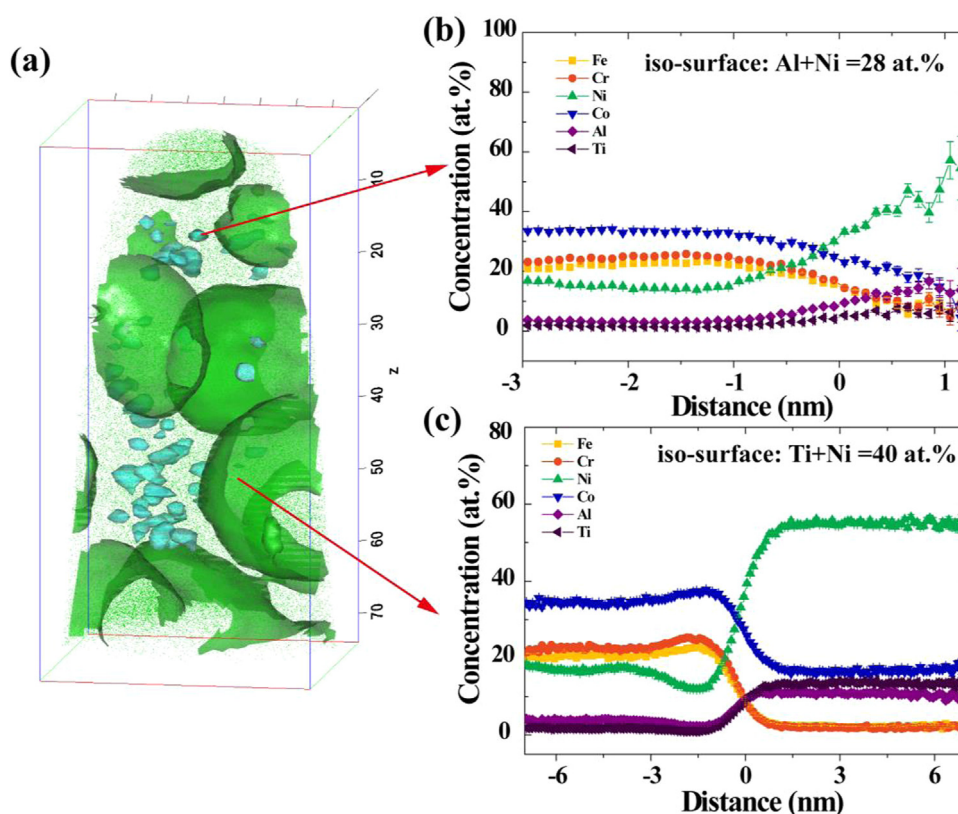


Fig. 4. (a) 3D reconstruction of an APT needle from the peak damaged region. An isosurface of 40% Ti+Ni (in green) was used to delineate the ordered nanoparticles after irradiation, while an isosurface of 28 at% Al+Ni (in blue) represents the irradiation-induced re-precipitation of the nano-clusters in the matrix. (b) Corresponding chemical profiles are shown in (b) and (c), respectively.

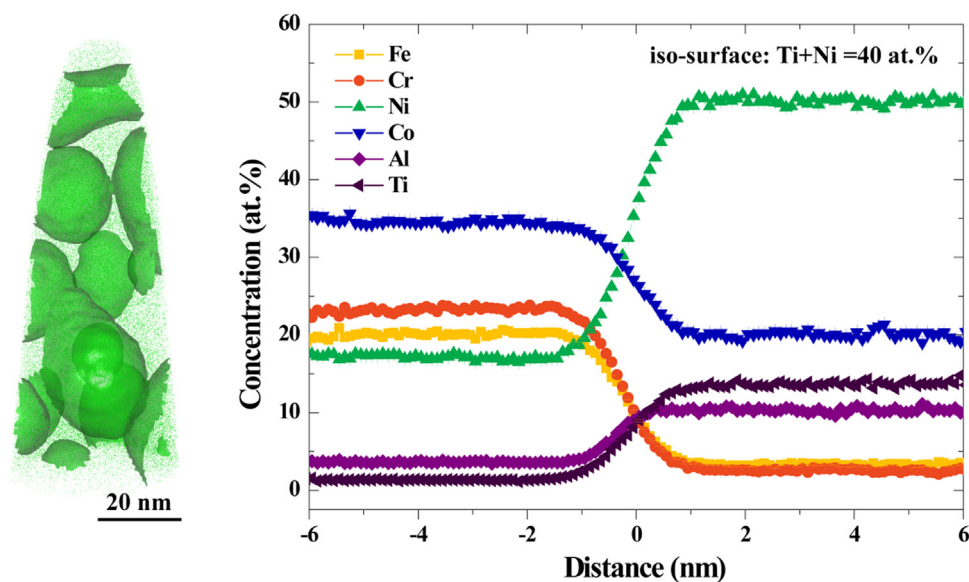


Fig. 5. Typical APT reconstruction of the underneath unirradiated region and the corresponding chemical profile across the matrix/precipitate interphase boundary.

To further quantitatively evaluate the RIS behavior of the He ion irradiated sample, a correlative TEM/APT measurement was conducted and the results are shown in Fig. 7. The BF-TEM images in Fig. 7(a, b) clearly show an SF and a target bubble (highlighted by a red dashed circle) in the APT specimen. The 2D projections of the Ni (at.%) and Co (at.%) compositional maps were shown in Fig. 7(c, d), respectively. As can be seen, there are a number of Ni-enriched regions dispersed in the matrix, which is correspond-

ing to the small clusters present in the 3D reconstruction in Fig. 4. The region with a strong Co enrichment that is connected to the phase boundary represents the bubble highlighted in Fig. 7(b), also marked with a circle in Fig. 7(d). Such a Co-enrichment is consistent with observations in Fig. 6. Apparently, the RIS occurs at both the SF plane and bubble surface. Fig. 7(e, f) displayed the chemical profile across the SF plane and the bubble, respectively, revealing a significant enrichment of Co (up to ~32 at.%) in the stacking fault

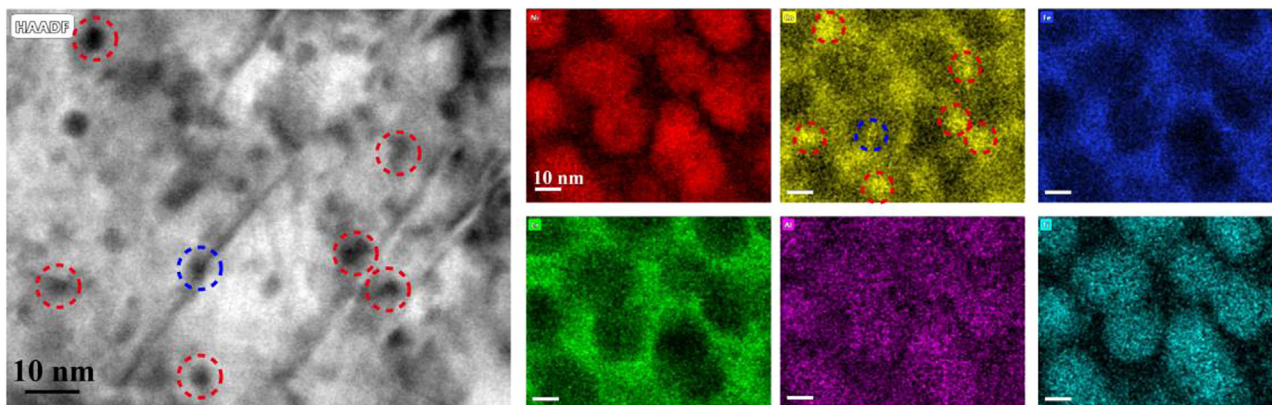


Fig. 6. STEM-HAADF image showing the distribution of He bubbles in dark contrast at the He implantation peak. EDS mapping of individual elements demonstrating the preferential entrapment of He bubbles at precipitate/matrix interface (highlighted by the red dashed circles). The bubble formed inside the L_{12} particle is marked with a blue dashed circle.

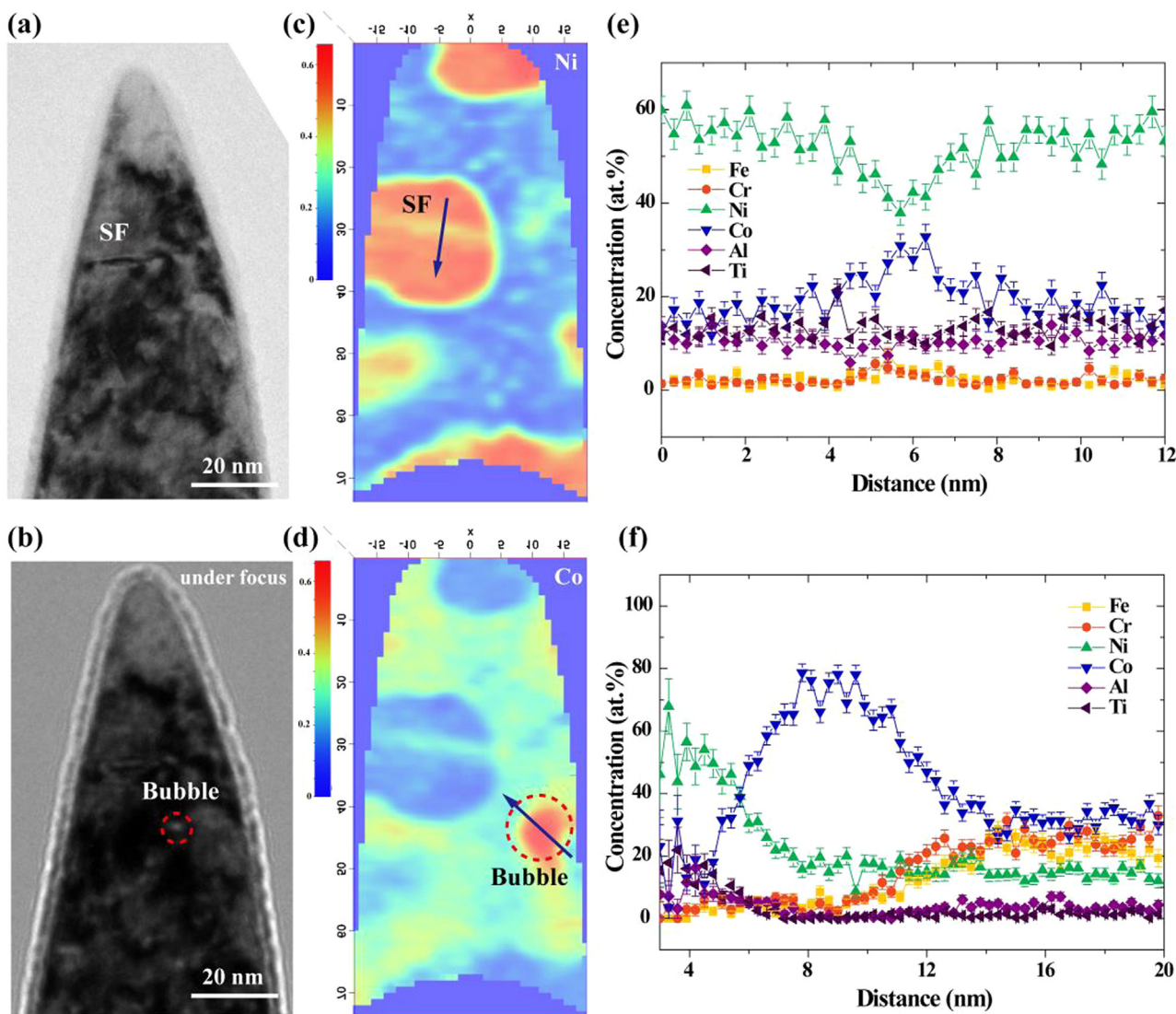


Fig. 7. Correlative TEM/APT investigation showing the location of helium bubbles in the peak damaged region of the irradiated Al_6Ti_6 . (a) On-focus BF-TEM image of the APT tip. (b) Corresponding under-focus BF-TEM image. (c) and (d) 2D projections of Ni and Co concentration maps, respectively, showing the segregation behaviors around the bubble. The thickness of the APT slices is 2 nm. An example of the bubble is indicated by red dashed circles in (d). The compositional profile along the direction marked by arrows in (c) and (d) showing the quantitative distribution of the elements perpendicular to SF plane (e) and across the bubble (f), respectively.

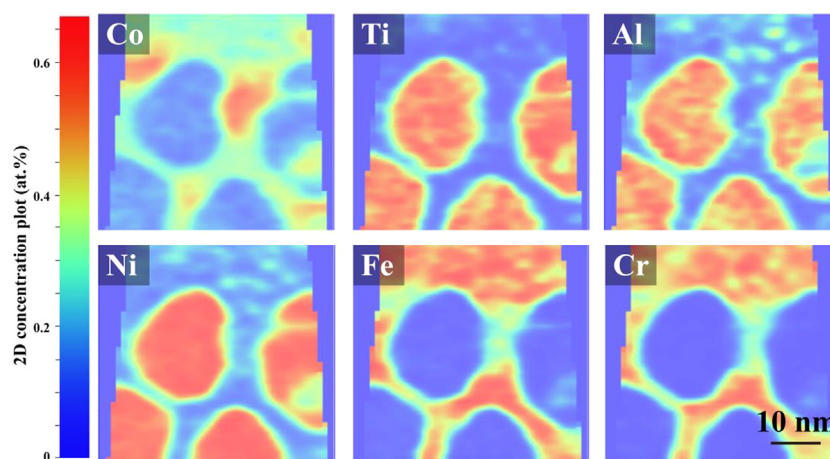


Fig. 8. 2D projections of the individual elements for an ATP slice (2 nm in thickness) in the peak damaged region of the irradiated Al6Ti6 HEA, showing the chemical redistribution under irradiation.

(SF) plane and even more striking segregation of Co at the bubble (up to ~ 78 at.%). Whereas, the Ni atoms are highly deficient at those sites. The significantly enriched Co element could further decrease the local stacking fault energy (SFE) around the SF region and is responsible for the retained large faulted loop displayed in Fig. 2.

4. Discussion

4.1. Helium entrapment on the coherent phase boundary

Helium atoms injected into metallic materials are easy to combine with vacancies, and consequently, aggregate and grow into bubbles [44]. Previous studies revealed that helium bubbles are likely to be trapped at vacancy-type defects [45], such as the interfaces and nanoclusters, etc. For the interphase-type sinks, i.e., grain boundaries and phase boundaries, the sink strength for He atom entrapment is highly correlated with the misfit dislocations intersections (MDIs) at those sites, i.e., the interface characters [13]. Han et al. [46] investigated the irradiation response of a He ion irradiated Cu at elevated temperature and proposed an elegant model to associate the width of the void-denuded zone of the $\Sigma 3$ $\langle 110 \rangle$ tilt grain boundary with the misorientation angle of the adjacent grains. They claimed that no void-denuded zone can be observed near the coherent twin boundary, implying a weak sink strength of this kind of coherent interface [46]. However, in the present HEA system, the coherent $L1_2$ /FCC interfaces show a considerable trapping efficiency of He bubbles (Figs. 6 and 7). Basically, such an enhanced He entrapment could be presumably due to the following reasons. First, the irradiation may cause a loss of interface coherency [47], which in turn serves as defect sinks as the incoherent interface. Yet no obvious evidence can be found to support this point in the present Al6Ti6 HEA, which could be ascribed to the insufficient damage level under He ion irradiation. More detailed studies in this regard are highly warranted. Second, the coherency stress raised from the lattice misfit between the precipitates and the matrix may promote defect migration towards the interfaces [48], resulting in the increased efficiency of He entrapment.

In addition, several studies have indicated that the He entrapment capability of the coherent interface shows a clear size dependence [48,49]. One piece of supporting evidence is that the fully coherent Cu/Co interface with a smaller layer (< 5 nm) distance results in an enhanced irradiation resistance in terms of reduced bubble density [48]. Fig. 8 displayed two-dimensional reconstructions of individual elements for another APT slice from the peak damaged region. Though the average width of the FCC channel can

be calculated to be ~ 14 nm [50], some of them could be narrowed down to a few nanometers, see Fig. 8. Those sites could thus serve as effective sinks to trap and store He bubbles, inhibiting bubble growth. This is consistent with our observation of reduced bubble size as compared to the single-phase FeCoNiCr HEA, showing an enhanced irradiation resistance of the Al6Ti6 HEA.

4.2. Mechanisms on the RIS at helium bubbles

The forming helium bubbles then further act as secondary sinks for both irradiation-produced vacancies and self-interstitials, leading to the elemental redistribution, i.e., the so-called RIS [24]. Generally, the RIS behavior is associated with inverse Kirkendall mechanism (IKE) [51] and Interstitial Binding (IB) [51]. The former suggested that the diffusivities of the elements either via vacancies or interstitial atoms play a critical role in the evolution of RIS. The latter suggested that undersized atoms migrate toward and oversized ones diffuse away from sinks. In previous literature, both mechanisms supported the observations of RIS behaviors in single-phase FeCoNiCr [20] and FeCoNiCrMn HEAs, where the oversized Fe/Cr elements would be depleted and undersized Ni/Co elements prefer to be enriched at sinks (e.g., grain boundary, dislocation loops, and voids) [52]. In particular, it is reported that the magnitude of Co enrichment is close to that of the Ni element. Although a similar RIS at the bubble surface is discovered in the He ion irradiated FeCoNiCr HEA [38], the segregation degree changes significantly. As compared to the heavy-ion irradiation, He could enhance the segregation heterogeneity, resulting in a strong Co segregation, weak Ni segregation, and Fe and Cr depletion around the bubble. However, in the present Al6Ti6 HEA, though Co still appears to be enriched around the helium bubble, the behavior of the undersized Ni element behaves oppositely, see the notable Ni deficiency in Figs. 7 and 8, which is deviated from the prediction of the IB model.

For the IKE mechanism, since He atoms are most likely to combine with vacancies to form bubbles, elements that have a preferential flux in exchange with vacancy flux tend to segregate towards the sink, i.e., the bubbles [44]. Given that the ordered $L1_2$ phase exhibit a relatively low atomic mobility as compared to the disordered FCC phase [53], the relative diffusivities of elements in the ordered $L1_2$ phase must be considered in the present alloy. Note that in the ordered $L1_2$ phase, Ni defects including Ni vacancies and Ni antisite defects were generally the majority defects in the irradiated Ni_3Al -type phase [54], implying that Ni has the largest diffusion coefficient in the $L1_2$ phase. Whereas, Co is often suggested to be the slowest diffuser in many multicomponent alloys

and Ni-based alloys [55,56]. Moreover, the implanted He atoms can further retard Co diffusion due to the repulsive interaction between them [38]. Consequently, the fastest Ni element diffuses away and leaves an enrichment of Co, the slowest diffusing species, at sinks. In other words, the unexpected depletion of Ni element around the bubbles is driven by the inverse Kirkendall effect. However, noting that the increment in Ni concentration can be only found in the L_{12} particles, the net concentration of Ni in the matrix remains at 17.1 at.%, which is similar to that of the underneath unirradiated region (17.3 at.%). These results indicated that the IKE-induced Ni atom flow towards the matrix is largely consumed due to the formation of L_{12} nano-clusters. As a consequence, nearly unchangeable concentrations of those elements can be found in the matrix after irradiation (Fig. 4). More importantly, such substantial segregation of constituent elements at bubbles did not change the main microstructure (FCC+ L_{12}) of the present Al6Ti6 HEA. Instead, it may play a critical role in tailoring mechanical properties, e.g., triggering mechanical twinning-induced plasticity due to the reduced SFE because of the increased Co content, which could be an interesting concern and requires additional work in the future.

4.3. Dynamic evolution of the L_{12} precipitates for enhanced irradiation resistance

It is generally accepted that the phase stability under irradiation primarily depends on two competing dynamics. On one hand, the energetic atoms bombard the lattice and bring about ballistic mixing, leading to the disordering or dissolution of the precipitates [57]. On the other hand, it will also produce defects like interstitials and vacancy, and in turn enhance the diffusion of the specific elements, which together with thermally driven diffusion tend to promote reordering or re-precipitation [58]. During He atom irradiation in the present case, two processes involving dissolution and re-precipitation of the L_{12} precipitates occur simultaneously. A clear dissolution of the L_{12} precipitates can be observed in Figs. 3 and 8, which could be attributed to the ballistic mixing and the associated He enhanced heterogeneity of the IKE-dominated RIS (Fig. 8). The re-precipitation of the nano-clusters appears to be associated with a collective effect from both kinetics and thermodynamics. First, the solubility of the solvent element generally diminishes as the temperature decreases. Combined with the IKE-induced migration of L_{12} -forming elements like Ni, Al, and Ti towards the matrix, it is thus expected that the matrix in the current alloy at 500 °C is highly supersaturated. Second, the lattice misfit between the matrix and precipitates of the present Al6Ti6 HEA is quite small, i.e., ~0.16% [32], which assumes a remarkably low interfacial energy (~40 mJ/m²) [59] and enables a low nucleation barrier at the onset of precipitation [60]. Du et al. [27] suggested that both two factors are critical to the intriguing re-precipitation behavior of the nano-clusters under irradiation. They claimed that precipitates tend to be simply dissolved either in alloy systems with relatively large lattice misfits (e.g., L_{21} -precipitates in body-centered-cubic matrices) or with low solvent content (e.g., 1Al steel compared to 3Al steel). In addition, there are a great number of excess interstitials and vacancies that survived during the irradiation process, which would bring about the so-called irradiation-enhanced diffusion. This in turn accelerates the clustering of excessive L_{12} -forming elements (Ni, Al, and Ti) and promotes the re-precipitation process of the L_{12} nanoprecipitates. Generally, the beneficial effect of nanoparticles (particularly the semicoherent nanoparticles) on the irradiation tolerance would degrade gradually as the limited microstructural stability of the alloy [61]. Yet despite a slight dissolution of the L_{12} precipitates, the newly-formed L_{12} precipitates and their possible growth continue to mitigate radiation damage for a retained irradiation resistance. Such dynamic dissolution and re-precipitation of the L_{12}

particles in the present Al6Ti6 HEA, in turn, stabilize the desirable (FCC+ L_{12}) superlattice structure, which, to some extent, present a “self-healing-like” effect and could potentially maintain the excellent damage tolerance of the material over the operational lifetime of a reactor. Certainly, a further enhancement of irradiation resistance could be expected by a delicate modulation of the microstructure and irradiation conditions, such as the volume fraction of the particles, the lattice misfit, the irradiation temperatures, etc., which deserves systematic studies in the further.

5. Conclusions

In summary, we reported the irradiation response of an L_{12} -strengthened Al6Ti6 HEA irradiated with He ions at 500 °C. The structural damage, the radiation-induced segregation, and the phase stability of the L_{12} precipitates have been carefully evaluated. The main conclusions are shown as follows:

- (1) Numerous faulted dislocation loops with considerably large sizes can be found in the He-irradiated HEA, indicating a delayed loop growth as with the other single-phase HEAs.
- (2) A combined TEM and APT characterization revealed that compared to the single-phase FeCoNiCr HEAs, a reduced bubble size exhibits in the present L_{12} -strengthened HEA, implying that the presence of the L_{12} nanoprecipitates can retard the bubble growth and in turn promote an enhanced irradiation tolerance.
- (3) Further results demonstrate that the coherent precipitate/matrix interface exhibited a good trapping efficiency of He atoms could help to mitigate radiation damage for a reduced bubble size as the channel width becomes small.
- (4) The RIS of the L_{12} -strengthened Al6Ti6 HEA under He ion irradiation is quantitatively examined by APT analysis. The results show a strong Co segregation and Ni depletion around He bubbles, which could be attributed to the inverse Kirkendall mechanism.
- (5) Dynamic precipitates dissolution and re-precipitation occur to maintain the beneficial microstructure of L_{12} precipitates and chemical complex FCC matrix, demonstrating a potential “self-healing effect” for a sustainable irradiation tolerance.

Declaration of Competing Interest

All the authors declare that they have no known competing financial interests or personal relationships that could have appeared to influence the work reported in this work.

Acknowledgments

The authors from the Harbin Institute of Technology (Shenzhen) thank the financial support from the National Natural Science Foundation of China (No. 52101135) and the Shenzhen Science and Technology Program (No. RCB20210609103202012). The authors from the City University of Hong Kong greatly acknowledge the financial support from the National Natural Science Foundation of China (No. 52101151), the Hong Kong Research Grant Council (RGC) (Nos. CityU 21205621 and C1017-21G), the Guangdong Basic and Applied Basic Research Foundation (No. 2020A1515110647), and the Shenzhen Science and Technology Program (No. SGDX20210823104002016).

References

- [1] S.J. Zinkle, Advanced Materials for Future Nuclear Plants, November 29–30, 2007. <https://gcep.stanford.edu/pdfs/UVaodfDrAb3BdgerCpoy-w/10-Zinkle-GCEP-Workshop.pdf>.
- [2] K.L. Murty, I. Charit, J. Nucl. Mater. 383 (2008) 189–195.
- [3] T. Yang, Y.L. Zhao, W.P. Li, C.Y. Yu, J.H. Luan, D.Y. Lin, L. Fan, Z.B. Jiao, W.H. Liu, X.J. Liu, J.J. Kai, J.C. Huang, C.T. Liu, Science 369 (2020) 427–432.

- [4] Q.Q. Ding, Y. Zhang, X. Chen, X.Q. Fu, D.K. Chen, S.J. Chen, L. Gu, F. Wei, H.B. Bei, Y.F. Gao, M.R. Wen, J.X. Li, Z. Zhang, T. Zhu, R.O. Ritchie, Q. Yu, *Nature* 574 (2019) 223–227.
- [5] E.P. George, D. Raabe, R.O. Ritchie, *Nat. Rev. Mater.* 4 (2019) 515–534.
- [6] Z.F. Lei, X.J. Liu, Y. Wu, H. Wang, S.H. Jiang, S.D. Wang, X.D. Hui, Y.D. Wu, B. Gault, P. Kontis, D. Raabe, L. Gu, Q.H. Zhang, H.W. Chen, H.T. Wang, J.B. Liu, K. An, Q.S. Zeng, T.G. Nieh, Z.P. Lu, *Nature* 563 (2018) 546–550.
- [7] H. Luo, Z.M. Li, A.M. Mingers, D. Raabe, *Corros. Sci.* 134 (2018) 131–139.
- [8] S.S. Nene, M. Frank, K. Liu, S. Sinha, R.S. Mishra, B.A. McWilliams, K.C. Cho, *Scr. Mater.* 166 (2019) 168–172.
- [9] Y.W. Zhang, G.M. Stocks, K. Jin, C.Y. Lu, H.B. Bei, B.C. Sales, L.M. Wang, L.K. Béland, R.E. Stoller, G.D. Samolyuk, M. Caro, A. Caro, W.J. Weber, *Nat. Commun.* 6 (2015) 8736.
- [10] Z. Fan, S.J. Zhao, K. Jin, D. Chen, Y.N. Osetskiy, Y.Q. Wang, H.B. Bei, K.L. More, Y.W. Zhang, *Acta Mater.* 164 (2019) 283–292.
- [11] Y.P. Lu, H.F. Huang, X.Z. Gao, C.L. Ren, J. Gao, H.Z. Zhang, S.J. Zheng, Q.Q. Jin, Y.H. Zhao, C.Y. Lu, T.M. Wang, T.J. Li, *J. Mater. Sci. Technol.* 35 (2019) 369–373.
- [12] X.H. Zhang, K. Hattar, Y.X. Chen, L. Shao, J. Li, C. Sun, K.Y. Yu, N. Li, M.L. Taheri, H.Y. Wang, J. Wang, M. Nastasi, *Prog. Mater. Sci.* 96 (2018) 217–321.
- [13] I.J. Beyerlein, M.J. Demkowicz, A. Misra, B.P. Uberuaga, *Prog. Mater. Sci.* 74 (2015) 125–210.
- [14] A. Konno, N.H. Oono, S. Ukai, S. Kondo, O. Hashitomi, A. Kimura, *Mater. Trans.* 58 (2017) 1636–1639.
- [15] P.D. Edmondson, C.M. Parish, Y. Zhang, A. Hallén, M.K. Miller, *Scr. Mater.* 65 (2011) 731–734.
- [16] K. Jin, C. Lu, L.M. Wang, J. Qu, W.J. Weber, Y. Zhang, H. Bei, *Scr. Mater.* 119 (2016) 65–70.
- [17] Y. Tong, G. Velisa, S. Zhao, W. Guo, T. Yang, K. Jin, C. Lu, H. Bei, J.Y.P. Ko, D.C. Pagan, Y. Zhang, L. Wang, F.X. Zhang, *Materialia* 2 (2018) 73–81.
- [18] T.F. Yang, W. Guo, J.D. Poplawsky, D.Y. Li, L. Wang, Y. Li, W.Y. Hu, M.L. Crespiello, Z.F. Yan, Y. Zhang, Y.G. Wang, S.J. Zinkle, *Acta Mater.* 188 (2020) 1–15.
- [19] C.Y. Lu, L.L. Niu, N.J. Chen, K. Jin, T.N. Yang, P.Y. Xiu, Y.W. Zhang, F. Gao, H.B. Bei, S. Shi, M.R. He, I.M. Robertson, W.J. Weber, L.M. Wang, *Nat. Commun.* 7 (2016) 1–8.
- [20] C.Y. Lu, T.N. Yang, K. Jin, N. Gao, P.Y. Xiu, Y.W. Zhang, F. Gao, H.B. Bei, W.J. Weber, K. Sun, Y. Dong, L.M. Wang, *Acta Mater.* 127 (2017) 98–107.
- [21] M.R. He, S. Wang, K. Jin, H.B. Bei, K. Yasuda, S. Matsumura, K. Higashida, I.M. Robertson, *Scr. Mater.* 125 (2016) 5–9.
- [22] Z. Wu, H. Bei, G.M. Pharr, E.P. George, *Acta Mater.* 81 (2014) 428–441.
- [23] T. Yang, Y.L. Zhao, Y. Tong, Z.B. Jiao, J. Wei, J.X. Cai, X.D. Han, D. Chen, A. Hu, J.J. Kai, K. Lu, Y. Liu, C.T. Liu, *Science* 362 (2018) 933–937.
- [24] B.X. Cao, W.W. Xu, C.Y. Yu, S.W. Wu, H.J. Kong, Z.Y. Ding, T.L. Zhang, J.H. Luan, B. Xiao, Z.B. Jiao, Y. Liu, T. Yang, C.T. Liu, *Acta Mater.* 229 (2022) 117763.
- [25] Y.J. Liang, L.J. Wang, Y.R. Wen, B.Y. Cheng, Q.L. Wu, T.Q. Cao, Q. Xiao, Y.F. Xue, G. Sha, Y.D. Wang, Y. Ren, X.Y. Li, L. Wang, F.C. Wang, H.N.A. Cai, *Nat. Commun.* 9 (2018) 4063.
- [26] Y.L. Zhao, T. Yang, Y.R. Li, L. Fan, B. Han, Z.B. Jiao, D. Chen, C.T. Liu, J.J. Kai, *Acta Mater.* 188 (2020) 517–527.
- [27] J.L. Du, S.H. Jiang, P.P. Cao, C. Xu, Y. Wu, H.Q. Chen, E.G. Fu, Z.P. Lu, *Nat. Mater.* (2022), doi:10.1038/s41563-022-01260-y.
- [28] Y.W. Zhang, X. Wang, Y.N. Osetsky, Y. Tong, R. Harrison, S.E. Donnelly, D. Chen, Y.Q. Wang, H.B. Bei, B.C. Sales, K.L. More, P.Y. Xiu, L.M. Wang, W.J. Weber, *Acta Mater.* 181 (2019) 519–529.
- [29] P.P. Cao, H. Wang, J.Y. He, C. Xu, S.H. Jiang, J.L. Du, X.Z. Cao, E.G. Fu, Z.P. Lu, *J. Alloy. Compd.* 859 (2021) 158291.
- [30] S.J. Zinkle, L.L. Snead, *Ann. Rev. Mater. Res.* 44 (2014) 241–267.
- [31] S.J. Zinkle, J.T. Busby, *Mater. Today* 12 (2009) 12–19.
- [32] T. Yang, Y.L. Zhao, J.H. Luan, B. Han, J. Wei, J.J. Kai, C.T. Liu, *Scr. Mater.* 164 (2019) 30–35.
- [33] J.F. Ziegler, M.D. Ziegler, J.P. Biersack, *Nucl. Instrum. Methods Phys. Res. Sect. B-Beam Interact. Mater. Atoms* 268 (2010) 1818–1823.
- [34] D. Chen, S.J. Zhao, J.R. Sun, P.F. Tai, Y.B. Sheng, Y.L. Zhao, G. Yeli, W.T. Lin, S.F. Liu, W. Kai, J.J. Kai, *J. Nucl. Mater.* 526 (2019) 151747.
- [35] D.B. Williams, C.B. Carter, *Transmission Electron Microscopy: A Textbook For Materials Science*, Springer Science-Business Media, New York, 2009.
- [36] S.F. Liu, *Helium Irradiation Defects and Mechanical Behavior of FCC-type Multicomponent Alloys*, City University of Hong Kong, 2021 Ph.D. Thesis.
- [37] M. Song, M. Wang, X.Y. Lou, R.B. Rebak, G.S. Was, *J. Nucl. Mater.* 513 (2019) 33–44.
- [38] W.T. Lin, G.M. Yeli, G. Wang, J.H. Lin, S.J. Zhao, D. Chen, S.F. Liu, F.L. Meng, Y.R. Li, F. He, Y. Lu, J.J. Kai, *J. Mater. Sci. Technol.* 101 (2021) 226–233.
- [39] F.C. Wu, Y.B. Zhu, Q. Wu, X.Z. Li, P. Wang, H.A. Wu, *J. Nucl. Mater.* 496 (2017) 265–273.
- [40] X.X. Wu, S.K. Makineni, C.H. Liebscher, G. Dehm, J. Rezaei Mianroodi, P. Shanthraj, B. Svendsen, D. Bürger, G. Eggeler, D. Raabe, B. Gault, *Nat. Commun.* 11 (2020) 1076.
- [41] P. De Almeida, R. Schäublin, A. Almazouzi, M. Victoria, M. Döbeli, *Appl. Phys. Lett.* 77 (2000) 2680.
- [42] G. Yeli, D. Chen, K. Yabuuchi, A. Kimura, S.F. Liu, W.T. Lin, Y.L. Zhao, S.J. Zhao, J.J. Kai, *J. Nucl. Mater.* 540 (2020) 152364.
- [43] Y. Hidaka, S. Ohnuki, H. Takahashi, S. Watanabe, *J. Nucl. Mater.* 212–215 (1994) 330–335.
- [44] B. Kombariah, P.D. Edmondson, Y. Wang, L.A. Boatner, Y. Zhang, *J. Nucl. Mater.* 514 (2019) 139–147.
- [45] P.D. Edmondson, C.M. Parish, Y. Zhang, A. Hallén, M.K. Miller, *J. Nucl. Mater.* 434 (2013) 210–216.
- [46] W.Z. Han, M.J. Demkowicz, E.G. Fu, Y.Q. Wang, A. Misra, *Acta Mater.* 60 (2012) 6341–6351.
- [47] L.M. Brown, G.R. Woolhouse, U. Valdrè, *Philos. Mag.* 17 (2006) 781–789.
- [48] Y. Chen, Y. Liu, E.G. Fu, C. Sun, K.Y. Yu, M. Song, J. Li, Y.Q. Wang, H. Wang, X. Zhang, *Acta Mater.* 84 (2015) 393–404.
- [49] Y.X. Chen, E.G. Fu, K.Y. Yu, M. Song, Y. Liu, Y.Q. Wang, H.Y. Wang, X.H. Zhang, *J. Mater. Res.* 30 (2015) 1300–1309.
- [50] R.W. Kozar, A. Suzuki, W.W. Milligan, J.J. Schirra, M.F. Savage, T.M. Pollock, *Metall. Mater. Trans. A-Phys. Metall. Mater. Sci.* 40 (2009) 1588–1603.
- [51] A.J. Ardell, P. Bellon, *Curr. Opin. Solid State Mat. Sci.* 20 (2016) 115–139.
- [52] C.M. Barr, J.E. Nathaniel, K.A. Unocic, J. Liu, Y. Zhang, Y. Wang, M.L. Taheri, *Scr. Mater.* 156 (2018) 80–84.
- [53] C.T. Liu, *Int. Met. Rev.* 29 (1984) 168–194.
- [54] F. Gao, D.J. Bacon, *Philos. Mag. A-Phys. Condens. Matter Struct. Defect Mech. Prop.* 67 (1993) 289–306.
- [55] Y.L. Zhao, T. Yang, B. Han, J.H. Luan, D. Chen, W. Kai, C.T. Liu, J.J. Kai, *Mater. Res. Lett.* 7 (2019) 152–158.
- [56] C.K.L. Davies, P. Nash, R.N. Stevens, *J. Mater. Sci.* 15 (1980) 1521–1532.
- [57] R.S. Nelson, J.A. Hudson, D.J. Mazey, *J. Nucl. Mater.* 44 (1972) 318–330.
- [58] K.Y. Liou, P. Wilkes, *J. Nucl. Mater.* 87 (1979) 317–330.
- [59] T. Yang, Y.L. Zhao, L. Fan, J. Wei, J.H. Luan, W.H. Liu, C. Wang, Z.B. Jiao, J.J. Kai, C.T. Liu, *Acta Mater.* 189 (2020) 47–59.
- [60] S.H. Jiang, H. Wang, Y. Wu, X.J. Liu, H.H. Chen, M.J. Yao, B. Gault, D. Ponge, D. Raabe, A. Hirata, M.W. Chen, Y.D. Wang, Z.P. Lu, *Nature* 544 (2017) 460–464.
- [61] T.R. Allen, J. Gan, J.I. Cole, S. Ukai, S. Shutthanandan, S. Thevuthasan, *Nucl. Sci. Eng.* 151 (2017) 305–312.